

Reynolds number scaling of flow in a stirred tank with Rushton turbine. Part II — Eigen decomposition of fluctuation

R. Raju^a, S. Balachandar^{a,*}, D.F. Hill^b, R.J. Adrian^a

^aDepartment of Theoretical & Applied Mechanics, University of Illinois, 216 Talbot Laboratory, 104 South Wright Street, Urbana, IL 61801 2983, USA

^bDepartment of Civil & Environmental Engineering, 212 Sackett Building, Pennsylvania State University, University Park, PA 16802, USA

Received 4 November 2003; received in revised form 4 November 2004; accepted 23 December 2004
Available online 4 March 2005

Abstract

We consider the question of scaling of flow within a stirred tank with increasing Reynolds number. Experimental results obtained from two different tanks of diameter 15.25 and 29.21 cm with a Rushton turbine operating at a wide range of rotational speed is considered for the scaling analysis. The resulting Reynolds number of the flow ranges from 4000 to about 80,000. Phase locked stereoscopic PIV measurements have been performed in order to obtain all three components of velocity on three different vertical planes close to the impeller. The scaling of plane-averaged mean flow was explored in the companion part-I of the paper. The scaling of rms and skewness of fluctuation about the mean is investigated here. The fluctuation about the mean is explained in terms of time-dependent oscillation of the impeller-induced jet and tip vortex components of the flow. The spatial structure of the instantaneous fluctuation about the mean is investigated in terms of eigenmodes obtained using proper orthogonal decomposition with the method of snapshots. The scaling of energy content of the dominant eigenmodes with Re is investigated.

© 2005 Published by Elsevier Ltd.

Keywords: Rushton turbine; Turbulence; Mixing; Scaling; Particle image velocimetry; Proper orthogonal decomposition

1. Introduction

A good understanding of the scaling of flow and mixing within a stirred tank reactor is of great importance in the process of scale-up from a gallon-sized laboratory experiment to a huge production-scale plant. Advances in experimental techniques have made detailed measurements of the mean and fluctuating flow field within the tank possible (Desouza and Pike, 1972; Van't Riet and Smith, 1975; van der Molen and van Maanen, 1978; Kolar et al., 1984; Costes and Couderc, 1988; Dong et al., 1994; Sturesson et al., 1995; Stoots and Calabrese, 1995; Ducoste et al., 1997; Kemoun et al., 1998; Lamberto et al., 1999; Montante et al., 1999; Mahouast et al., 1989; Schaffer et al., 1997; Derksen et al.,

1999; Escudie and Line, 2003; Escudie et al., 2004; Yoon et al., 2001). Several of these investigations have addressed the question of scaling by making velocity measurements inside stirred tanks of varying size, over a range of operating speeds and thus covering a range of Reynolds number (Desouza and Pike, 1972; Van't Riet and Smith, 1975; van der Molen and van Maanen, 1978; Kolar et al., 1984; Costes and Couderc, 1988; Dong et al., 1994; Sturesson et al., 1995; Stoots and Calabrese, 1995; Ducoste et al., 1997; Kemoun et al., 1998; Lamberto et al., 1999; Montante et al., 1999). The focus has mostly been on the scaling of time- or phase-averaged mean quantities, primarily the mean velocity, and to some extent on other quantities such as mean dissipation and strain rate (Costes and Couderc, 1988; Stoots and Calabrese, 1995). The impeller diameter and the blade tip velocity are observed to be the appropriate scales and at high enough Reynolds numbers the mean flow quantities appropriately nondimensionalized become Reynolds number independent.

* Corresponding author. Tel.: +1 217 244 4371; fax: +1 217 244 9090.
E-mail address: s-bala@uiuc.edu (S. Balachandar).

In comparison, our understanding of fluctuation about the mean and its scaling is limited. In a turbulent flow stirring and mixing by the large- and small-scale fluctuations are quite important, and thus it is necessary to understand the scaling of fluctuation, as well as the mean flow. Complete characterization of the fluctuation requires statistical information such as the standard deviation, skewness, and other higher order moments. The root mean square (rms) fluctuation of the radial, circumferential and axial velocity components have been observed to scale with blade tip velocity (Costes and Couderc, 1988; Dong et al., 1994; Sturesson et al., 1995; Ducoste et al., 1997; Kemoun et al., 1998). No reliable information exists on higher order statistics. The recent investigation of Kemoun et al. (1998) has also considered the scaling of Reynolds stress, however in the low Re range.

The proper orthogonal decomposition (POD) methodology provides a convenient and the most efficient way to characterize the instantaneous fluctuation about the mean. This methodology has been shown to be successful in the characterization of a variety of turbulent flows (Holmes et al., 1996). The eigenfunctions obtained from the POD methodology systematically characterize how the instantaneous flow fields depart in their spatial structure from the mean field, and the corresponding eigenvalues represent the energy content in those modes.

Here we will use results from experiments performed in two different tanks over varying impeller speeds covering a Reynolds number range from 4000 to 80,000. Stereoscopic particle image velocimetry (SPIV) measurements within the tank provide accurate measurements of all three components of velocity. In the companion paper by Yoon et al. (2005) (henceforth will be addressed as Y-I) we addressed the scaling of the ensemble averaged mean flow and its spatial dependence.

This paper will address the nature of fluctuation and how it varies with increasing tank size and operating speed of the impeller. The scaling of the energy content of the dominant eigenmodes, with respect to increasing Re is considered. In particular, the approach to Reynolds number independence for the appropriately nondimensionalized quantities will be determined. The spatial structure of the dominant eigenfunctions for the varying cases is obtained to evaluate their dependence on Reynolds number.

2. Experimental set-up

The diameters of the small and the large circular tanks are $T_1 = 152.5$ mm and $T_2 = 292.1$ mm, respectively. Both the tanks are unbaffled and filled with de-ionized water to a depth equal to the diameter. A lid was placed at the top to suppress any free-surface effect that might otherwise become significant at higher rotational speeds. The two tanks are geometrically similar, so that dynamic similarity can also be achieved at matching Reynolds numbers. A Rushton turbine,

having a diameter one-third the tank diameter ($D = T/3$), was mounted at mid-depth along the axis of the cylinder. The shaft was extended through the impeller to the bottom of the tank and held in place by a bearing to eliminate ‘wobble’ of the impeller. The impellers used in the large and small tanks are geometrically scales, except for subtle deviation in the blade and disk thickness (see Y-I (Yoon et al., 2005)). The Reynolds numbers, defined as $Re = ND^2/\nu$ (N is blade rotations per second, D is the impeller diameter and ν is the kinematic viscosity of the fluid), varied from 4293 to 63,066 for the small tank and from 4229 to 78,308 for the large tank.

SPIV was used to obtain all three components of velocity on three vertical parallel planes slightly outside the cylindrical surface swept by the impeller. An optical encoder was used to trigger each data acquisition phase-locked with the same impeller blade location. The timing of data acquisition was chosen to be precisely midway between two adjacent blades, so that the vertical planes of measurement symmetrically covered the 60° sector between the impeller blades. For the small tank these planes (near, mid and far planes) were located at 23.22, 25.13, and 27.67 mm from the impeller shaft and for the large tank these planes were located at 45.12, 48.77, and 53.64 mm (see Fig. 1). For each combination of impeller speed and acquisition plane, 500 realizations were obtained. For further details on the apparatus and the experimental procedure the reader is referred to the part I of this paper (Y-I (Yoon et al., 2005)).

3. Proper orthogonal decomposition

The instantaneous data obtained on the vertical planes from the stereoscopic PIV measurements will be denoted as $\mathbf{u}^{(l)}(y, z)$, where the superscript indicates the l th realization (see Fig. 1 for coordinate definition). The above planar measurements are in the y - z plane at three different distances from axis of the impeller. The measurements are made phase-locked with the blade location such that they approximately cover a 60° sector between the two blades. The phase-averaged mean velocity field, $\langle \mathbf{u} \rangle(y, z)$, can be defined as an average over an ensemble of L realizations and correspondingly the perturbation away from the mean is given by

$$u_i^{(l)}(y, z) = u_i^{(l)}(y, z) - \langle u_i \rangle(y, z) \quad \text{where} \\ \langle u_i \rangle(y, z) = \frac{1}{L} \sum_{l=1}^L u_i^{(l)}(y, z). \quad (1)$$

We now look for a candidate orthonormal basis set, $\Psi_i^{(n)}(y, z)$, for the optimal representation of the perturbation field as an expansion given by

$$u_i^{(l)}(y, z) = \sum_n a^{(l,n)} \Psi_i^{(n)}(y, z), \quad (2)$$

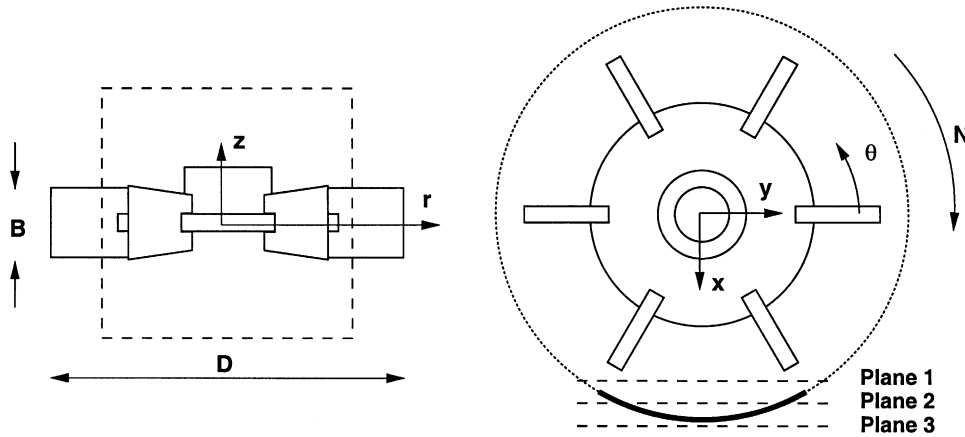


Fig. 1. Schematic of the region close to the impeller showing the three vertical parallel planes on which the PIV measurements were taken.

where the sum is over the complete set of the orthonormal basis and the scalars $a^{(l,n)}$ are the eigencoefficients of the n th basis for the l th realization. We define the basis such that the above eigenexpansion is optimal for the representation of the energy content. This requirement can be translated into the following Fredholm integral equation of the second kind for the optimal expansion basis (Holmes et al., 1996):

$$\int \int \mathbf{R}_{ij}(y, z, y^*, z^*) \Psi_j^{(n)}(y^*, z^*) dy^* dz^* = \lambda^{(n)} \Psi_i^{(n)}(y, z), \quad (3)$$

where the integral is over the entire y - z plane. The kernel of the integral equation is the two point correlation tensor of the perturbation field defined as

$$\mathbf{R}_{ij}(y, z, y^*, z^*) = \langle u_i^{(l)} u_j^{(l)} \rangle = \frac{1}{L} \sum_{l=1}^L u_i^{(l)}(y, z) u_j^{(l)}(y^*, z^*). \quad (4)$$

The domain of integration is finite, and the kernel, by definition, is real symmetric and positive definite. From the theory of symmetric integral equations (Mikhlin, 1957) the above integral equation has a discrete set of solutions with the eigenfunctions, $\Psi_i^{(n)}(y, z)$, and the associated eigenvalues, $\lambda^{(n)}$, enumerated and denoted by the superscript, $n = 1, 2, \dots, \infty$. The eigenfunctions form a complete set of square-integrable orthonormal functions satisfying

$$\int \int \Psi_i^{(m)}(y, z) \Psi_i^{\dagger(n)}(y, z) dy dz = \delta_{m,n}, \quad (5)$$

where the superscript ‘ \dagger ’ indicates a complex conjugate. The eigenvalues measure the mean square energy content in that mode as

$$\frac{1}{L} \sum_{l=1}^L a^{(l,m)} a^{\dagger(l,n)} = \lambda^{(n)} \delta_{m,n} \quad (6)$$

and the above equation also shows that the different eigencoefficients are uncorrelated. The eigenmodes can be rank ordered in terms of $\lambda_1 > \lambda_2 > \dots > \lambda_n > \dots$, such that the energy content of the mode decreases with the mode number. The optimality of the expansion guarantees that the convergence of $\sum_{n=1}^N \lambda^{(n)}$ with increasing N to the total energy is faster than any other expansion.

3.1. Method of snapshots

On each vertical plane, for each Reynolds number, the experimental data set consists of 500 individual measurements that extend in the axial direction on either side of the midplane ($z = 0$). Note that all quantities to be presented are nondimensionalized with distances scaled by the blade tip radius and velocities scaled by the blade tip velocity. For each individual measurement an equally admissible realization can be constructed with the following symmetry:

$$\begin{aligned} u(y, z) &\rightarrow u(y, -z), \\ v(y, z) &\rightarrow v(y, -z), \\ w(y, z) &\rightarrow -w(y, -z), \end{aligned} \quad (7)$$

where u , v , and w are the velocities along the x , y , and axial directions. Thus the total size of the extended ensemble used in the computation of the two-point correlation tensor is $L = 1000$. Extending the ensemble in this way forces the statistics to be symmetric about $z = 0$.

The PIV measurements are typically discretized on a grid. Here we employ a uniform grid of 61×28 points to discretize the symmetrized measurement region of $-0.67 < y < 0.67$ and $0 < z < 0.6$ for the small tank and a uniform grid of 75×31 points to discretize the region $-0.65 < y < 0.65$ and $0 < z < 0.51$ for the large tank. As a result of this spatial discretization, the two-point correlation tensor becomes a large matrix of size 5124 and 6975 for the small and large tanks, respectively. Correspondingly, the integral equation (3) becomes a matrix eigenvalue problem. The ensemble

size, $L = 1000$, used in the construction of the two-point correlation tensor, is smaller than the matrix size, $P = 5124$ or 6975 . Since the two-point correlation is based on perturbation, its rank is one less than the size of the ensemble. As a result the number of independent eigenmodes is only $L - 1$. If the ensemble size, L , were to be larger than the matrix size, P , then the number of independent eigenmodes of the discrete system will be P .

As pointed out by Sirovich (1987) it is far simpler in problems where $L \ll P$ to follow an alternate formulation of the eigenvalue problem, known as the method of snapshots. In this approach the eigenfunctions are defined to be admixtures of the ensemble of realizations

$$\Psi_i^{(n)}(y, z) = \sum_{l=1}^L b^{(n,l)} u_i^{(l)}(y, z). \quad (8)$$

where $b^{(n,l)}$ are the weighting coefficients. Thus the $L - 1$ nontrivial eigenmodes of the problem result from the $L - 1$ independent linear combinations of all the realizations. The above can be thought of as an inverse of the expansion shown in Eq. (2). For the case when $L < P$ the eigenmodes as defined in the method of snapshots (Eq. 8) are fully consistent with those defined by the Fredholm integral equation (3). However, when $L > P$, the above definition is incompatible with the eigenmodes arising from the two-point spatial correlation.

Analogous to the two-point spatial correlation, the two-time correlation tensor can be defined as

$$\mathbf{T}^{(m,n)} = \frac{1}{J} \frac{1}{K} \sum_{j=1}^J \sum_{k=1}^K u_i^{(m)}(y_j, z_k) u_i^{(n)}(y_j, z_k), \quad (9)$$

where y_j and z_k are the discrete points along the y and z directions where the velocity measurements were made and J and K denote the total number of discrete points in these directions. In the continuous representation the above summations will be replaced by spatial integrals along y and z . Also in the above equation it is assumed that the discrete points of velocity measurement are equi-spaced (as in the present experiments), for otherwise appropriate weights must be assigned to each data point in the summation. The eigenvalue problem analogous to the one given in Eq. (3) can now be written in terms of the two-time correlation as

$$\frac{1}{L} \sum_{l=1}^L \mathbf{T}^{(m,l)} b^{(n,l)} = \lambda^{(n)} b^{(n,m)}, \quad n = 1, 2, \dots, L - 1. \quad (10)$$

Here we have computed the eigenmodes from both the spatial formulation given in Eq. (3) and the method of snapshots. Both the methods yield identical results and in general the method of snapshots is preferred owing to its computational speed.

4. Results

The individual perturbation fields on the three vertical planes are uncorrelated, as they are taken at different instances in time. As a result, interpolation on to a cylindrical surface as was carried out in Y-I (Yoon et al., 2005), for the perturbation velocity, is not meaningful. Thus statistics such as rms velocity, skewness, and eigenmodes need to be computed on the three vertical planes individually. Here, we present the results on the vertical planes without any interpolation. Since the results on the different planes for varying Re are qualitatively similar, only a subset will be presented.

4.1. rms velocity scaling

The rms fluctuation field for the three components of velocity on each measurement plane is defined as follows:

$$\sigma_i(y, z) = \left[\frac{1}{L} \sum_{l=1}^L (u_i^{(l)}(y, z))^2 \right]^{1/2}. \quad (11)$$

Figs. 2(a–c) shows the rms fluctuation field for the three components of velocity on the vertical plane closer to the axis (near plane) for the small tank at $Re = 4300$. Here, and in what follows, all quantities to be presented are nondimensionalized with the blade tip radius as the length scale and the blade tip velocity as the velocity scale. Figs. 3(a–c) shows the rms fluctuation fields for the vertical plane closer to the axis (near plane) for the small tank at the highest Reynolds number of $Re = 63,180$ considered. The u'_2 and u'_3 components are fluctuations on the measurement plane along the y and z directions, while u'_1 is the fluctuating component normal to the plane of measurement. Therefore, u'_3 represents the axial velocity fluctuation, while u'_2 and u'_1 correspond to circumferential and radial fluctuations only midway between the blades, i.e., at $y = 0$. At other locations the circumferential and radial components of the velocity fluctuation can be extracted from u'_1 and u'_2 as

$$\begin{aligned} u'_r &= u'_3 \frac{y}{\sqrt{y^2 + x_p^2}} + u'_1 \frac{x_p}{\sqrt{y^2 + x_p^2}} \quad \text{and} \\ u'_\theta &= u'_3 \frac{x_p}{\sqrt{y^2 + x_p^2}} - u'_1 \frac{y}{\sqrt{y^2 + x_p^2}}, \end{aligned} \quad (12)$$

where x_p is the normal distance from the axis of the tank to the plane of measurement.

It can be seen from Figs. 2 and 3 that the peak velocity fluctuations in the radial and circumferential components are of comparable magnitude, while in comparison the peak axial velocity fluctuation is somewhat weaker. In all cases the strongest fluctuation is close to the midplane ($z = 0$) and around $y \approx -0.3$. Based on the mean flow results presented in Y-I (Yoon et al., 2005) this is about the location where the tip vortex pair intersects the plane of measurement. Thus, the strongest velocity fluctuation is associated

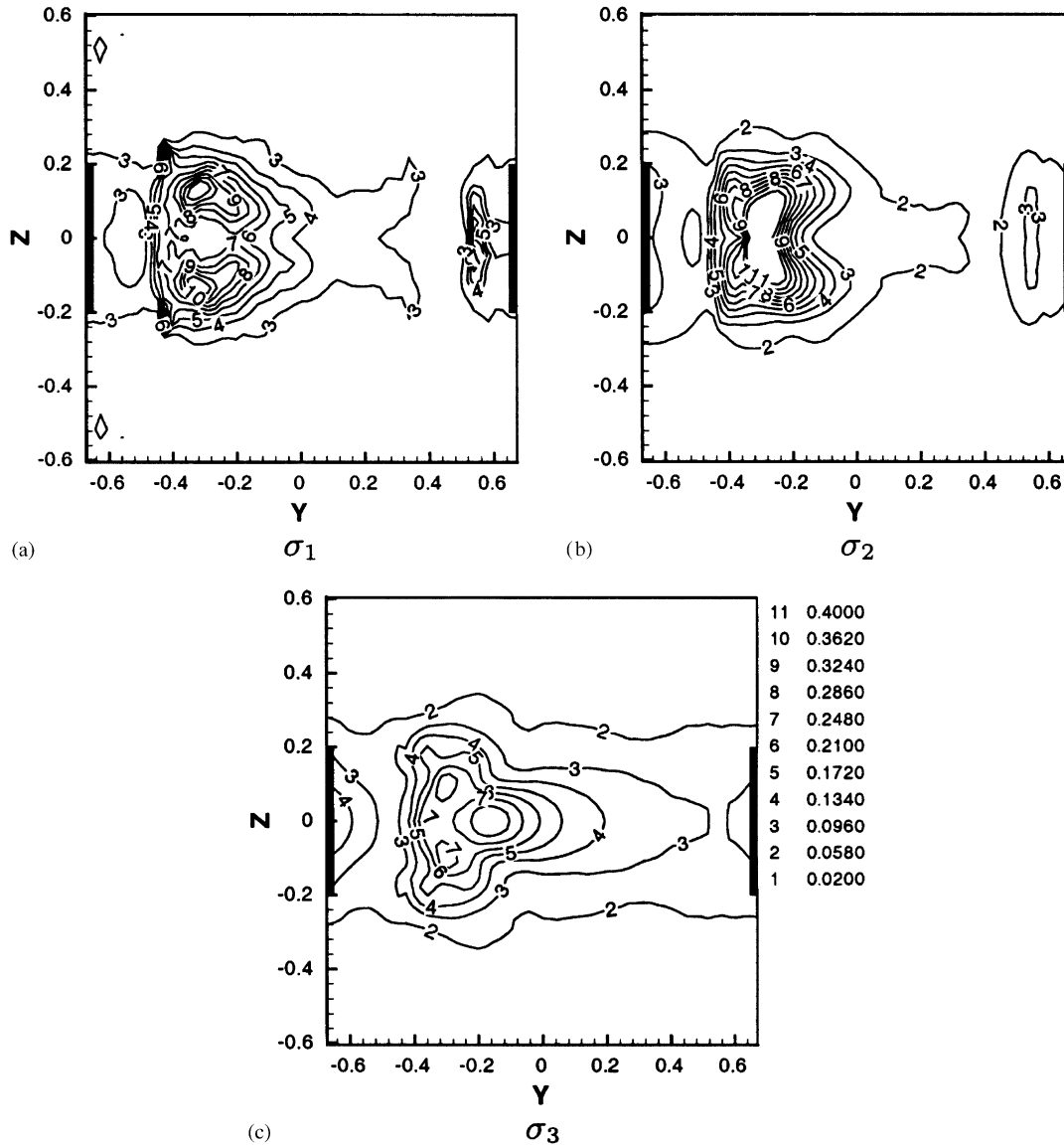


Fig. 2. RMS fluctuation field for the vertical plane closer to the axis (near plane) for the small tank at $Re = 4300$ (the thick lines indicate the locations of the impeller blades).

with the time-dependence of the tip vortex system. The radial and circumferential velocity fluctuations decay rapidly away from the tip vortex pair, while the axial component of velocity fluctuation (u'_3) appears to extend away from the tip vortex pair, but remains focused close to the axial midplane ($z = 0$). Note that the noise close to $y \approx 0.5$ in u'_1 and to a lesser extent in u'_2 is due to reflection from the blade tip. Figs. 4(a–c) shows the rms fluctuation field on the vertical plane closer to the axis (near plane) for the large tank at $Re = 4229$. Figs. 5(a–c) shows the corresponding rms fluctuation fields for the large tank at $Re = 78,308$. From the figures, it is clear that rms velocity fields for the large tank are qualitatively similar to those seen for the small tank.

The scaling of rms fluctuation is investigated in Fig. 6 with a plot of $\overline{\sigma'_i}$ vs Reynolds number for both the small

and the large tank, where the double overbar indicate a y – z surface average. Fig. 6a shows the result obtained at the near plane, while Fig. 6b shows the results for the far plane. Fluctuation of the out-of-plane velocity component, u'_1 , averaged over the plane is about 70–80% higher than the in-plane velocity fluctuation. The higher rms fluctuation at the lower Reynolds numbers is consistent with the detailed distribution shown in Figs. 2–5, where the peak values of rms velocity fluctuation can be seen to be substantially lower at the higher Reynolds numbers. The rms fluctuation statistics appear to approach Reynolds number independence, but the approach is somewhat slower on the far plane in comparison to the near plane. As with the mean flow the normalized rms statistics of the two tanks do not perfectly collapse even at large Re , and this difference is most visible in $\overline{\sigma'_1}$.

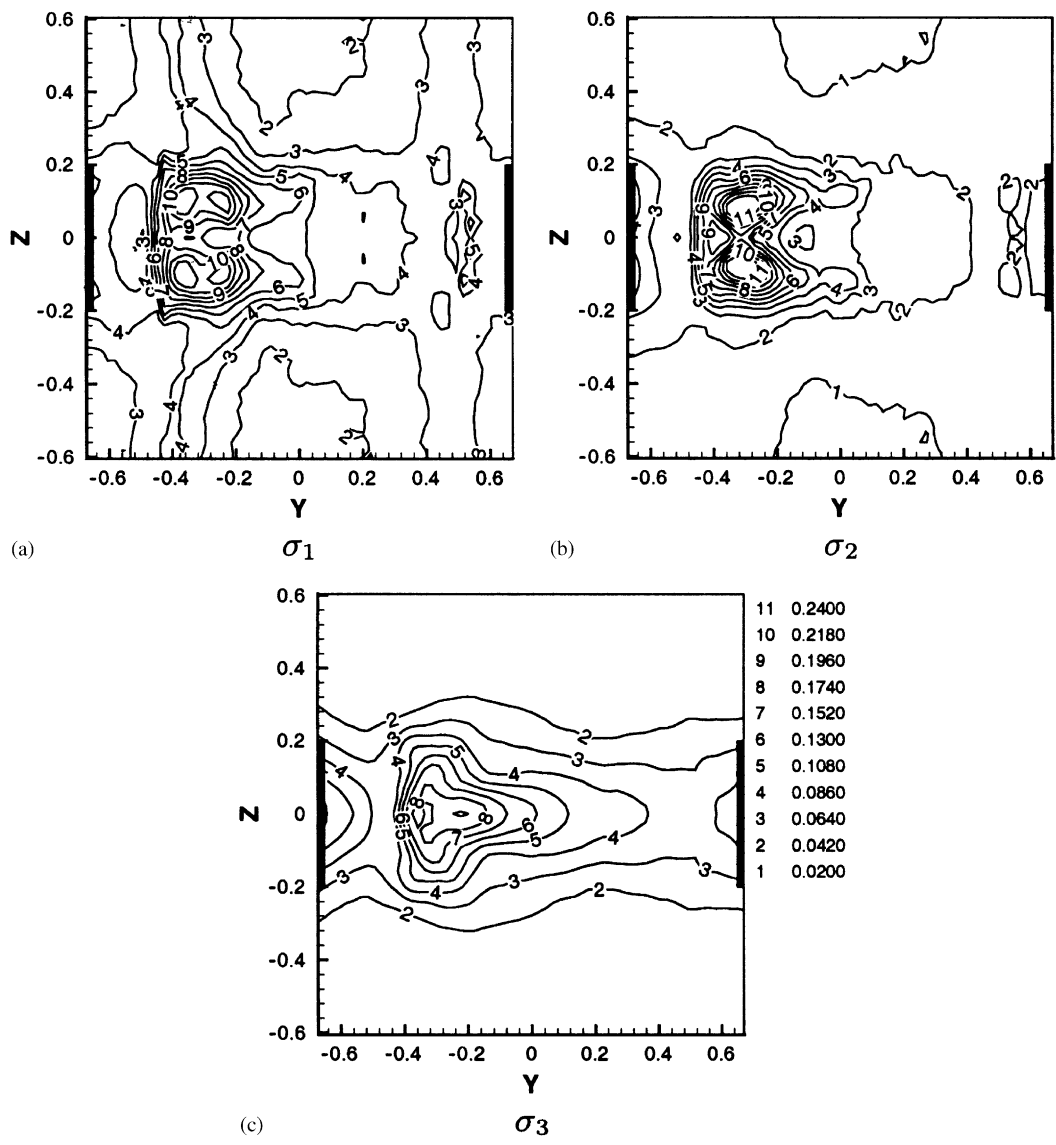


Fig. 3. RMS fluctuation field for the vertical plane closer to the axis (near plane) for the small tank at $Re = 63,180$.

4.2. Skewness scaling

The skewness of velocity fluctuation on the measurement plane is defined as

$$S_i(y, z) = \frac{\frac{1}{L} \sum_{l=1}^L (u_i^{(l)}(y, z))^3}{\sigma_i^{3/2}} \tag{13}$$

Fig. 7a shows the distribution of skewness of the axial component of velocity on the vertical plane closer to the axis (near plane) for the small tank at $Re = 63,180$ and the corresponding result for the large tank at $Re = 78,308$ is shown in Fig. 7b. At the lower Reynolds numbers velocity skewness is qualitatively similarly distributed, and therefore it is not shown. The skewness results are somewhat noisy away from the midplane ($z = 0$) of the tank, since the velocity fluctua-

tions are themselves quite small there. From Fig. 7 it is clear that the skewness of the axial velocity is asymmetrically distributed about the midplane ($z = 0$), and it reaches a local peak value in the region of the tip vortex pairs. Away from the influence of the tip vortices, the distribution of skewness is consistent with the up and down motion of the jet component of the impeller flow. Fig. 8 shows the Reynolds number scaling of the peak skewness for the two different tanks in the near plane. Here peak skewness is identified in the region of the tip vortices (note that the peak value is chosen here instead of planar average, since the later is influenced by noise seen away from the midplane).

4.3. Jet oscillation model

The flow out of the impeller zone for the Rushton turbine can be considered as a superposition of circumferential flow,

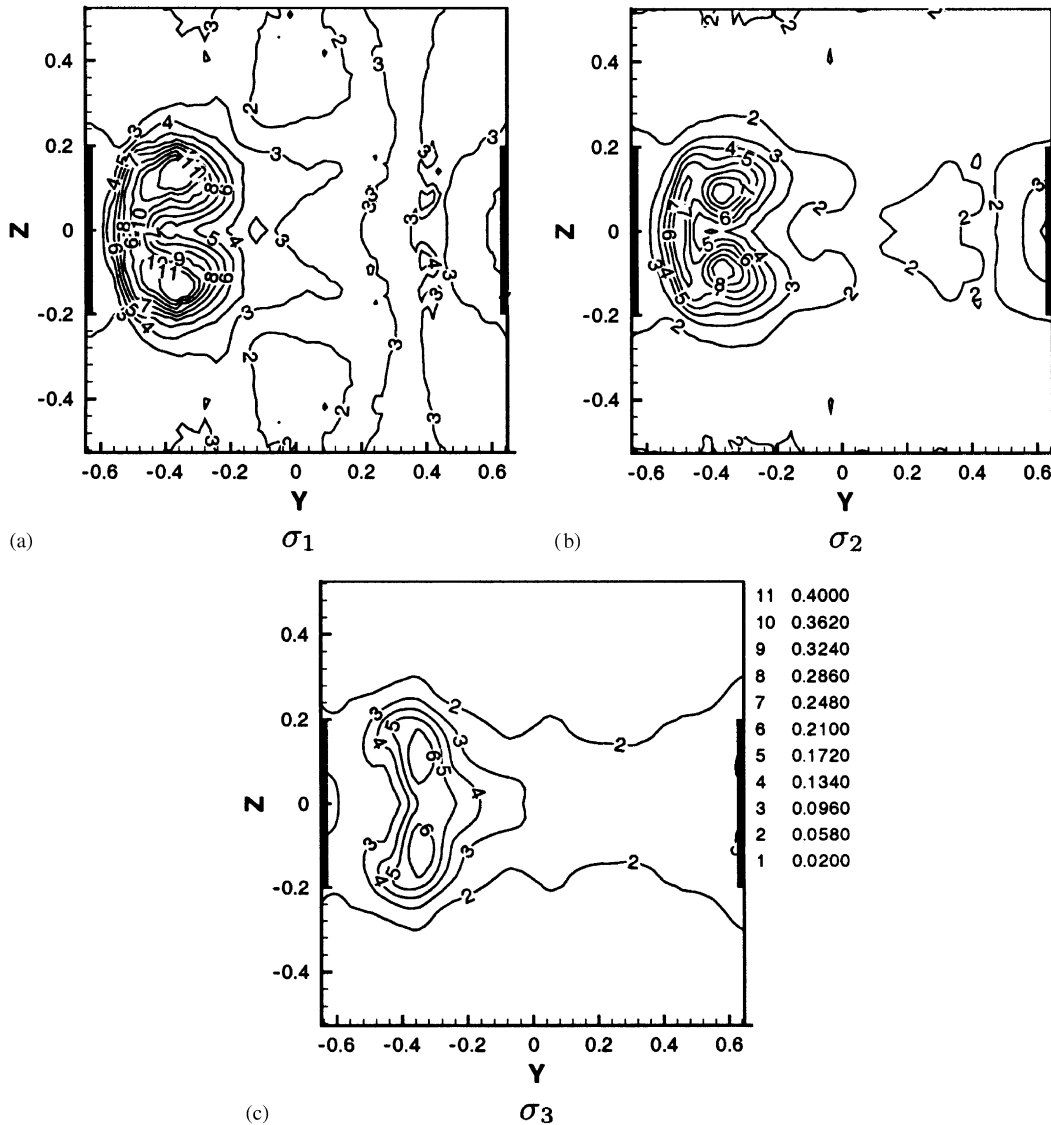


Fig. 4. RMS fluctuation field for the vertical plane closer to the axis (near plane) for the large tank at $Re = 4229$.

circular jet and pairs of tip vortices (Yoon et al., 2001). It was further conjectured in Yoon et al. (2003) that the time-dependent nature of the impeller-induced flow is primarily due to the time-dependence of the jet flow and the tip vortex components. In particular, it was shown that by accounting for the time-dependent nature of the jet flow as an up and down oscillation about the midplane, the flow in the interior of the tank could be more accurately computed (see Fig. 9 for a schematic). The pattern of fluctuating axial velocity, u'_3 , seen away from the location of the tip vortex pair ($y \approx 0.3-0.6$) will be now used to investigate this time-dependent nature of the jet flow.

A theoretical model for the jet component of the impeller-induced flow assumes the jet to be purely circumferential at the virtual origin of the jet, but progressively turn towards the radial direction. The thin shear-layer approximation can be used to obtain an analytic description of the jet flow Yoon

et al. (2001). The jet flow will be considered to be axisymmetric and dependent on the radial distance from the axis of the jet, ξ , and the transverse distance from the jet centerplane, ζ . On the centerplane of the jet the angle θ_J the flow makes with the radial direction is given by $\theta_J = \cos^{-1} \left[\sqrt{\xi^2 - a^2/\xi} \right]$. The radial and circumferential jet velocities are given by

$$\begin{aligned}
 u_\xi &= U_J \{1 - \tanh^2 \eta\} \cos(\theta_J) \quad \text{and} \\
 u_\theta &= U_J \{1 - \tanh^2 \eta\} \sin(\theta_J),
 \end{aligned}
 \tag{14}$$

where the centerline velocity, U_J , and the self-similar axial distance, η , are given by

$$U_J = \frac{A}{\sqrt{\xi}} \frac{1}{(\xi^2 - a^2)^{1/4}} \quad \text{and} \quad \eta = \frac{\sigma \zeta}{(\xi^2 - a^2)^{1/2}}.
 \tag{15}$$

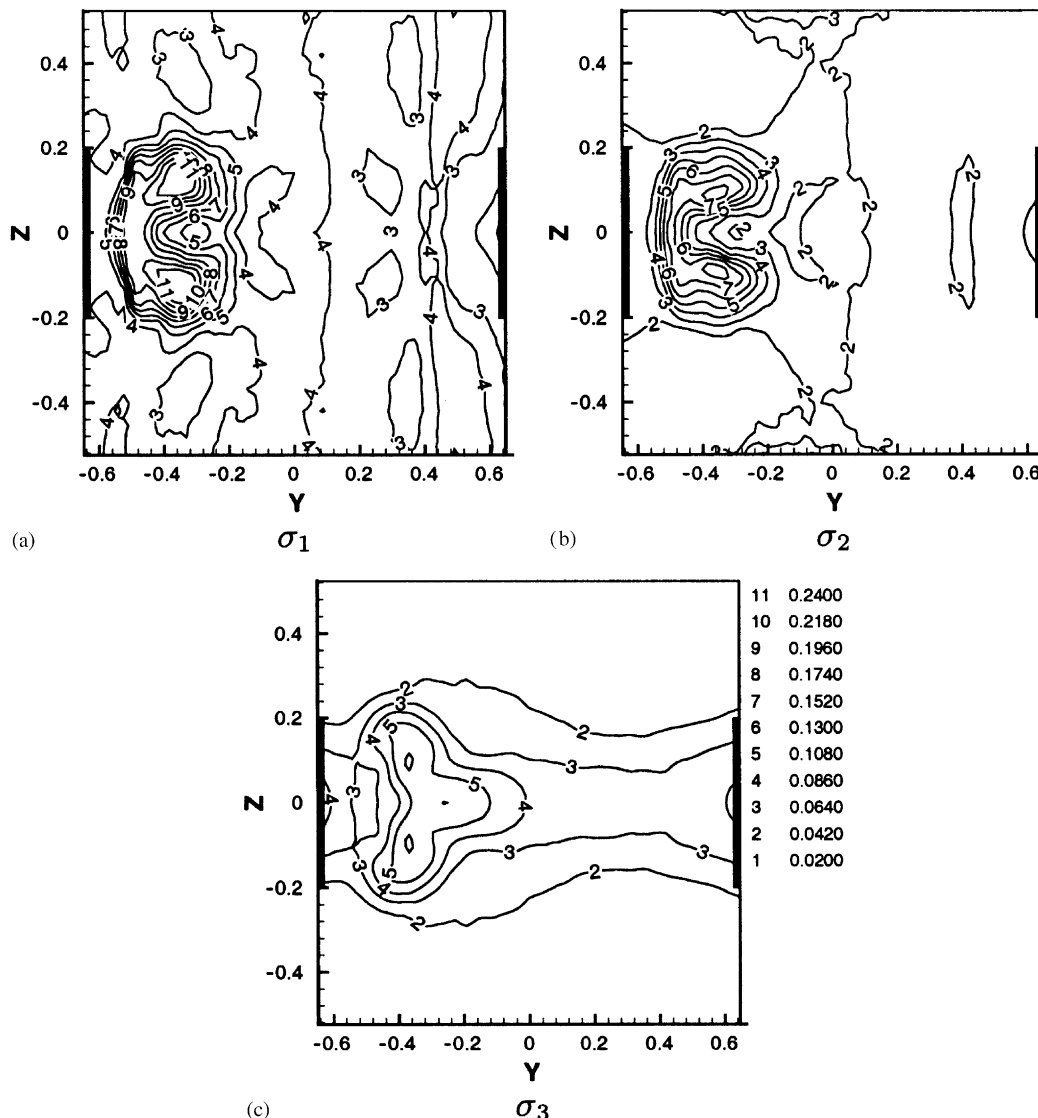


Fig. 5. RMS fluctuation field for the vertical plane closer to the axis (near plane) for the large tank at $Re = 78,308$.

The corresponding transverse velocity induced by entrainment is given by continuity as

$$u_\zeta = U_J \left\{ \frac{z}{(\xi^2 - a^2)^{1/2}} [1 - \tanh^2 \eta] - \frac{(2\xi^2 + a^2)}{2\sigma\xi^2} \tanh \eta \right\}. \tag{16}$$

The jet is thus parameterized by A , the jet strength, σ , the inverse jet width and a , the radial location of the virtual origin from the axis.

We will estimate the effect of up and down oscillation of the jet flow about the midplane of the tank with a simplistic model. As seen by a fixed point rotating with the blade, the unsteadiness of the jet will be approximated as an up

and down tilting of the jet centerline about the tank mid-plane, pivoted about a virtual origin. The time-dependent angle between the two will be taken to be $\phi(t)$ (see Fig. 9). A fixed point in the rotating frame of reference, given by (r^*, z^*) , then sees a time-dependent influence of the jet with the radial and axial location within the jet in (13)–(15) varying as

$$\begin{aligned} \xi(t) &= [(r^* - a)^2 + z^{*2}]^{1/2} \cos \left[\tan^{-1} \left(\frac{z^*}{r^* - a} \right) - \phi(t) \right], \\ \zeta(t) &= [(r^* - a)^2 + z^{*2}]^{1/2} \\ &\quad \times \sin \left[\tan^{-1} \left(\frac{z^*}{r^* - a} \right) - \phi(t) \right]. \end{aligned} \tag{17}$$

Furthermore, as the jet oscillates the alignment of u_ξ and u_ζ of the jet with the radial and axial directions of the tank varies.

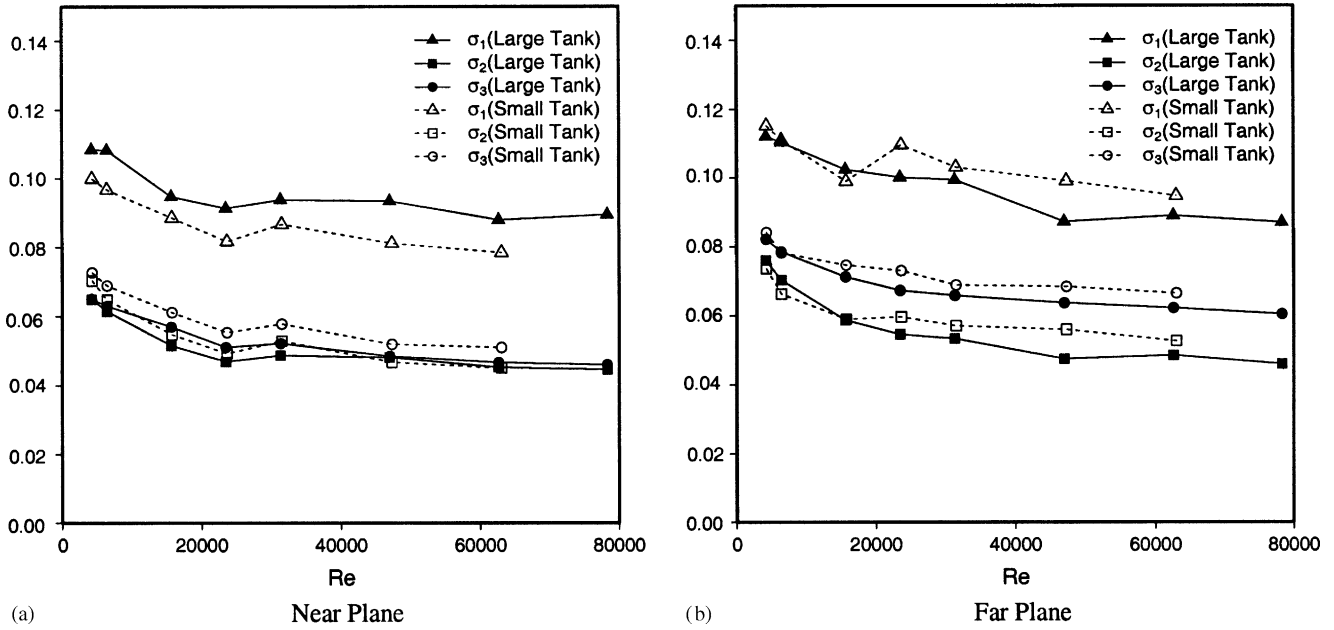


Fig. 6. Reynolds number scaling of y - z surface-averages rms fluctuation for both the small and large tanks.

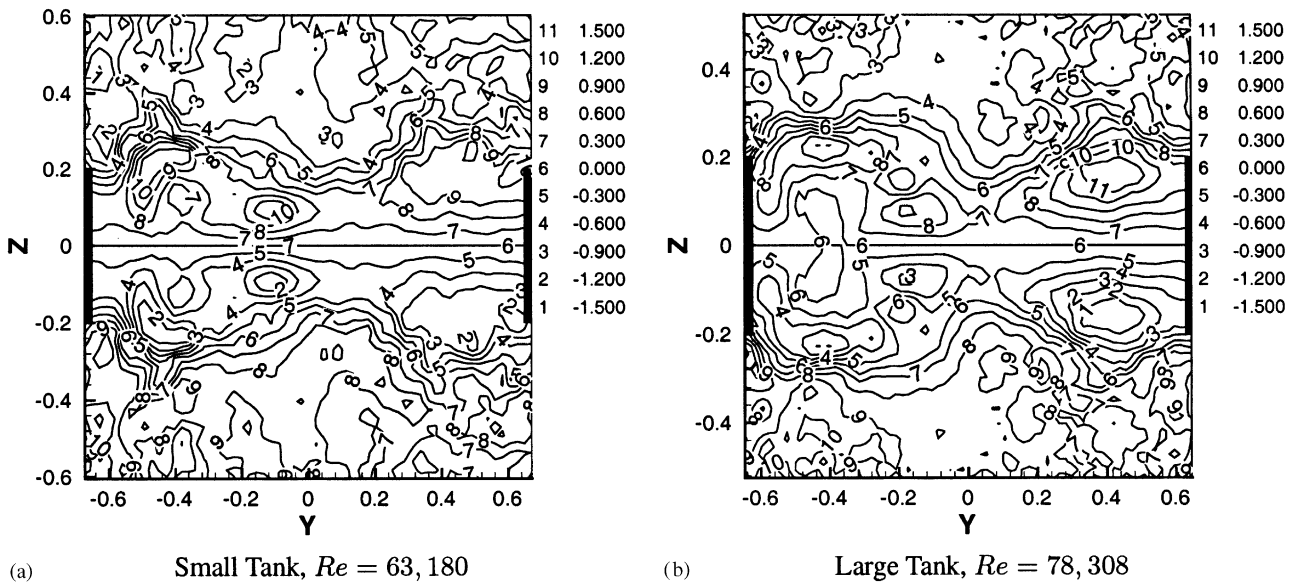


Fig. 7. Distribution of the skewness of the axial component of velocity on the vertical plane closer to the axis (near plane) for the small and the large tank.

A simple sinusoidal oscillation of the jet of the form, $\phi(t) = \phi_0 \sin(\omega t)$, is assumed, where ϕ_0 and ω are the amplitude and frequency of jet oscillation. A synthetic time history of velocity seen at a fixed point in the rotating frame of reference can be constructed with such an assumption. The time history of radial and axial velocities seen at a point located at $(r^* = 1, z^* = 0.1)$ for $\phi_0 = 10^\circ, 20^\circ$ and 30° are shown in Fig. 10. From such synthetic time histories various statistics can be computed. Fig. 11a shows the variation in rms fluctuation of radial and axial velocity components with z^* to be expected at a fixed radial distance of

$r^* = 1$, based on the above synthetic model of jet flow oscillation. The results from three different amplitudes of jet oscillation, $\phi_0 = 10^\circ, 20^\circ$ and 30° are shown and the results are independent of the oscillation frequency. It is clear that the axial velocity fluctuation is significantly larger than the radial velocity fluctuation. The circumferential velocity fluctuation (not shown here) is of the order of the radial velocity fluctuation. The behavior of the actual rms velocity fluctuations shown in Figs. 2–5, away from the influence of the tip vortices is consistent with the above model prediction.

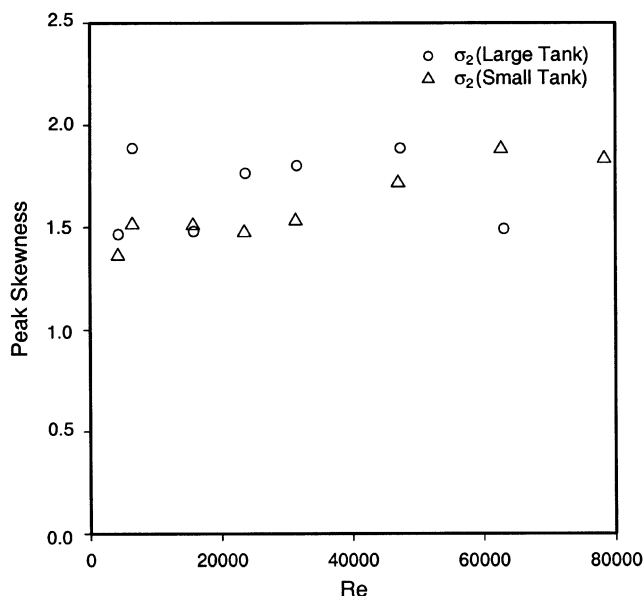


Fig. 8. Reynolds number scaling of skewness for the three components of velocity on the near plane for the small and the large tank.

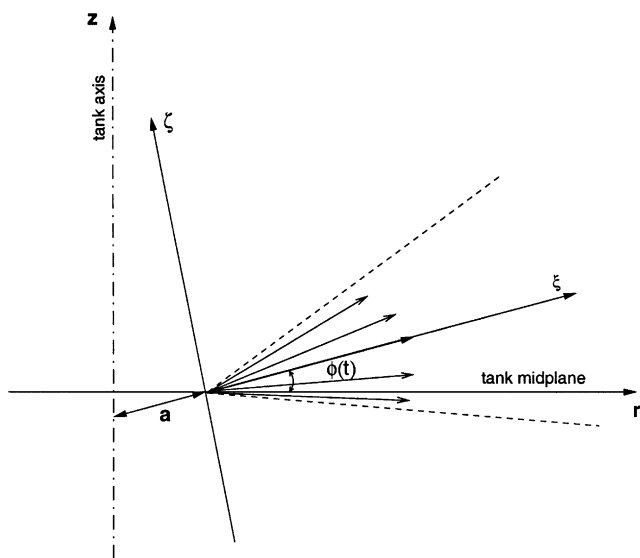


Fig. 9. Schematic of the theoretical jet model that is undergoing time-dependent oscillation.

Fig. 11b shows the corresponding variation in the skewness of axial velocity with z^* for the three different amplitudes of jet oscillation, $\phi_0 = 10^\circ, 20^\circ$ and 30° . These estimates of z -dependence of skewness can be compared with the actual axial variation of skewness seen in Fig. 7 around $y \approx 0.5$. Given the simplicity of the above model of jet oscillation, the magnitude and location of peak skewness are in reasonable qualitative agreement with the actual measurement. The qualitative agreement suggests that the measured velocity fluctuation can be partially attributed to the coherent oscillation of the impeller-induced jet component. Such

up and down oscillation of the jet can also be seen in time-dependent numerical simulations (Yoon et al., 2003) and also cinematographic PIV measurements (Kim, 2004).

4.4. Eigenmodes

In this section, we present the eigenmodes obtained with the method of snapshots. The most energetic eigenfunction represents the dominant structure of instantaneous departure from the mean and the second most energetic eigenfunction represents the next important structure of instantaneous departure and so on. Thus, it is of interest to investigate the similarity between the most energetic eigenmodes for varying Re and tank size.

Fig. 12 (frames a–c) shows the structure of the dominant eigenmode in terms of contours of in-plane and out-of-plane velocity components for the small tank at $Re = 4300$ obtained on the near plane. Frames d–f show the corresponding most energetic eigenmode for the small tank at the highest Reynolds number considered, $Re = 63,180$. Fig. 13 shows the corresponding most energetic eigenmode for the large tank at $Re = 62,646$. For all the three cases shown the qualitative similarity of the most energetic mode is evident and although not shown here, it remains similar for all the other cases considered as well. The in-plane velocity perturbation of the dominant mode represents a compact vortex centered about $y \approx -0.3$ and $z = 0$. The sense of rotation of the vortex changes from clockwise or counter-clockwise rotating depending on the sign of the corresponding eigencoefficient.

In the small tank the most energetic mode accounts for nearly 25% of the total energy at $Re = 4300$ (see Fig. 14), but its energy content steadily decreases with Reynolds number and at $Re = 63,180$ it accounts for only 16%. Also shown in Fig. 14 are the corresponding results for the large tank on the near plane. For the large tank with increasing Re the percentile energy content of the dominant mode appears to settle to a constant value of about 8.5%, while for the small tank an asymptotic state is not observed even at the highest Re considered.

Owing to the symmetry of the two-point correlation about the tank midplane ($z = 0$), the eigenmodes separate into even and odd modes (here we will determine the nature of the mode based on the out-of-plane component of velocity, u_1). As can be seen in Fig. 13 the dominant eigenmode is an odd mode with the out-of-plane velocity antisymmetric about the tank midplane. Thus the dominant mode does not alter the net instantaneous flow rate induced by the impeller, but only influences the top-bottom symmetry of the impeller-induced flow. In contrast, a symmetric mode will alter the net instantaneous flow rate induced by the impeller. Fig. 15 shows the contours of velocity components for the dominant symmetric mode for the small tank at $Re = 63,180$. The in-plane velocity corresponds to a pair of counter rotating vortices placed on either side of the midplane located around

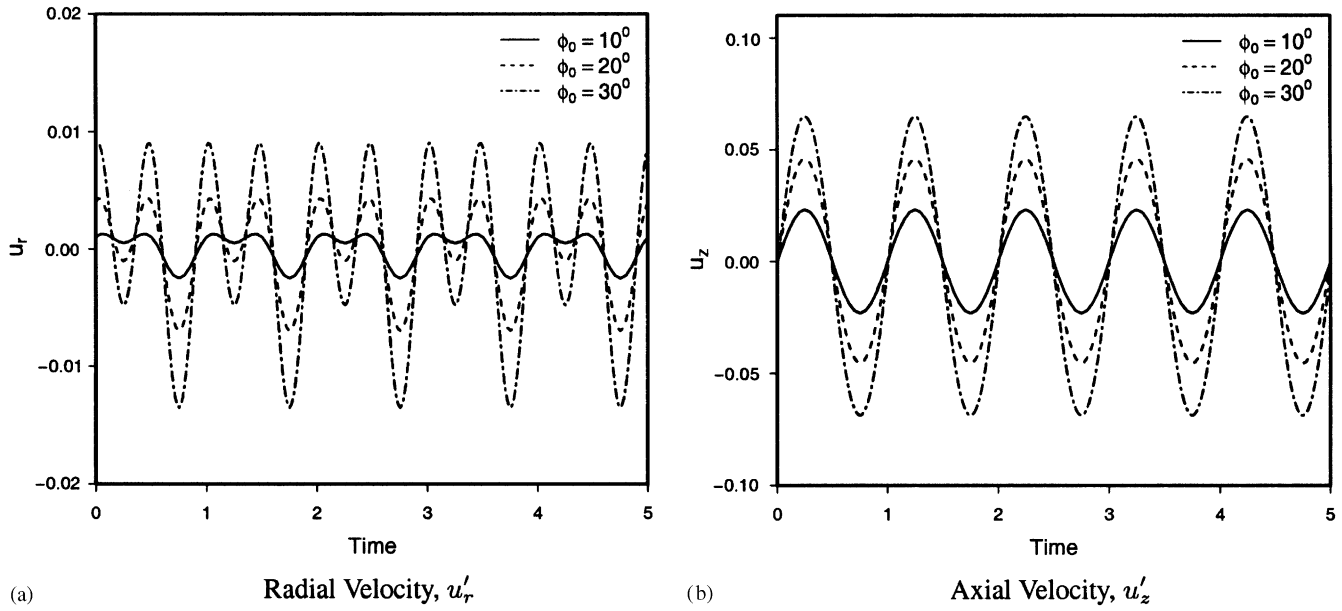


Fig. 10. Time history of the radial and axial velocities at point located at $(r^* = 1, z^* = 0.1)$.

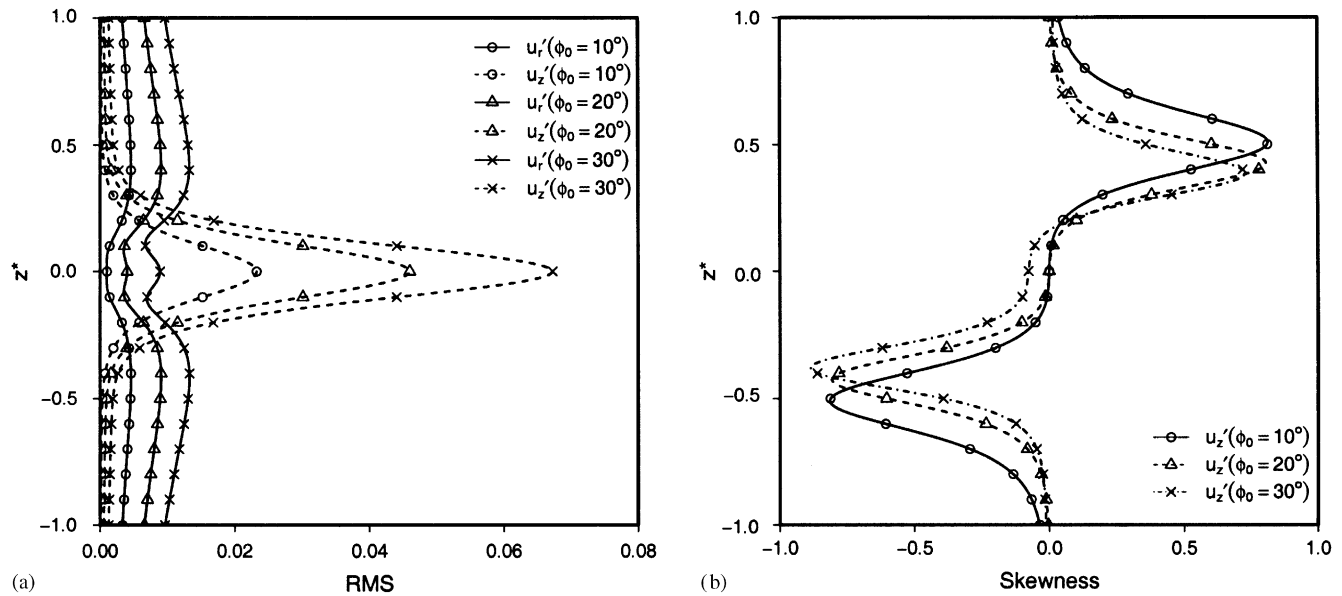


Fig. 11. Variation in (a) rms fluctuation of radial and axial velocities, (b) skewness of the axial velocity with z^* .

$y \approx -0.2$. The direction of out-of-plane velocity is related to the sense of rotation of the counter rotating vortices. If the direction of rotation of the counter rotating vortex pair is the same as the tip vortex component of the mean flow then the effect of the dominant symmetric mode is to increase the out-of-plane velocity along the tank midplane, and decrease it away from the midplane. However, as the amplitude and sign of the coefficient of the dominant symmetric mode varies over time the sense of rotation of the counter rotating vortices and their influence on the out-of-plane flow changes. Thus the dominant symmetric mode can be simply

interpreted as the time-dependent variation in the strength of the tip vortex pair.

Fig. 16 shows the Reynolds number dependence of the total energy content in the even and the odd modes for the small and large tanks. Almost Reynolds number independence can be observed for both the tanks. In the small tank, the symmetric (even) modes account for 60% of the total perturbation energy and the remainder is accounted by the asymmetric modes. In the large tank, the symmetric and asymmetric modes account for about 53% and 47% of the total energy, and thus are of approximately equal strength.

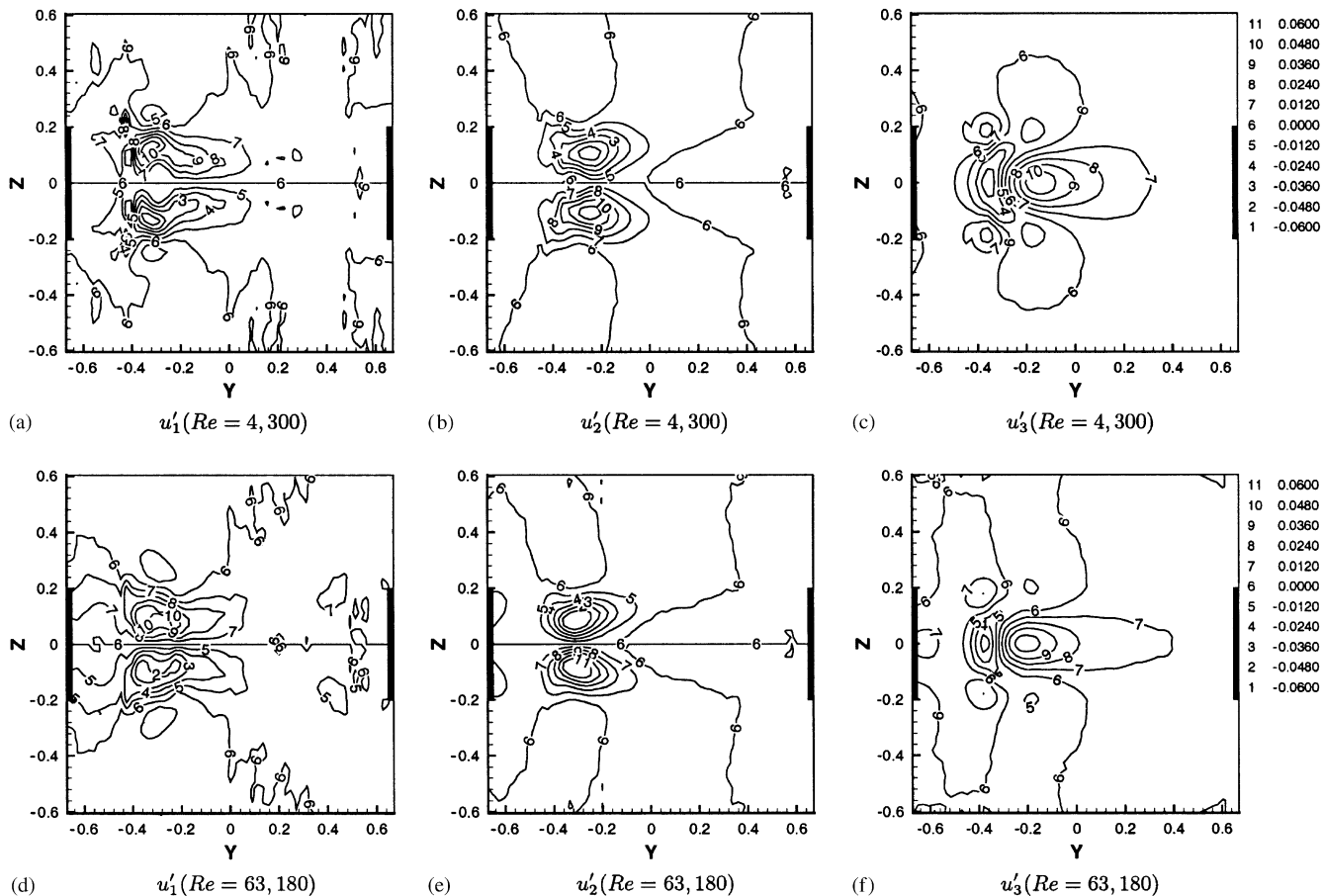


Fig. 12. Structure of the dominant eigenmode in terms of contours of velocity components for the small tank at two different Reynolds number.

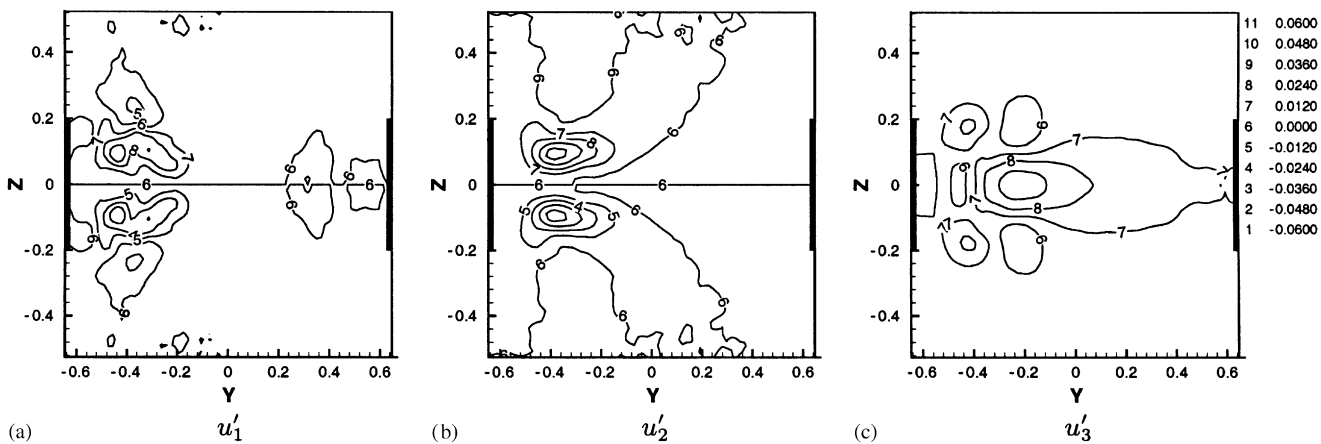


Fig. 13. Structure of the dominant eigenmode in terms of contours of velocity components for the large tank at $Re = 64,646$.

Fig. 17 shows the cumulative percentile energy in the dominant n modes, defined as

$$F(n) = \frac{\sum_{l=1}^n \lambda^{(l)}}{\sum_l \lambda^{(l)}} \tag{18}$$

where in the denominator the sum is over all the eigenmodes. As can be expected the convergence is more rapid at the lower Reynolds number and convergence slows down with increasing Reynolds number, as more energy is contained in the higher order modes. The trend for the small and large tanks, although similar, shows no-

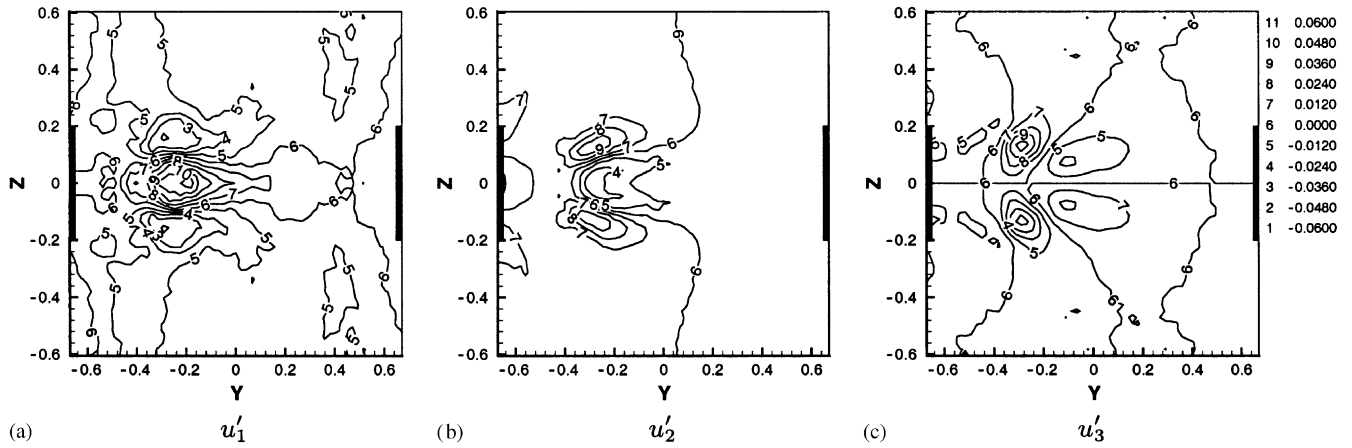


Fig. 15. Structure of the dominant symmetric eigenmode in terms of contours of velocity components for the small tank at $Re = 63,1806$.

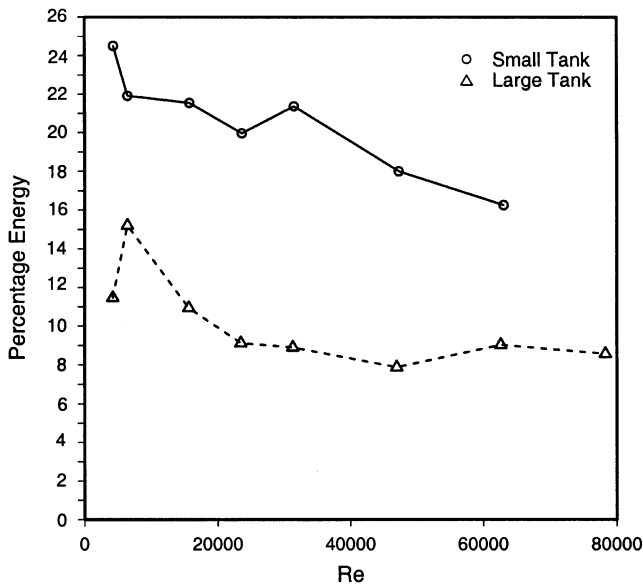


Fig. 14. Percentage energy contained in the most dominant eigenmode for the small and the large tank.

ticeable differences, especially at the higher Reynolds number.

5. Summary and conclusions

Phase-locked stereoscopic PIV measurements were made to obtain all three components of the impeller-induced flow on three different vertical planes that cover the 60° sector between two adjacent blades. An ensemble of 500 such measurements were taken from which the mean, rms and skewness of fluctuation about the mean were computed. The distribution of rms velocity fluctuation over the measurement plane indicate time-dependent behavior of the jet and tip vortex components of the impeller-induced flow. The rms fluctuation of each component of velocity, averaged over the plane

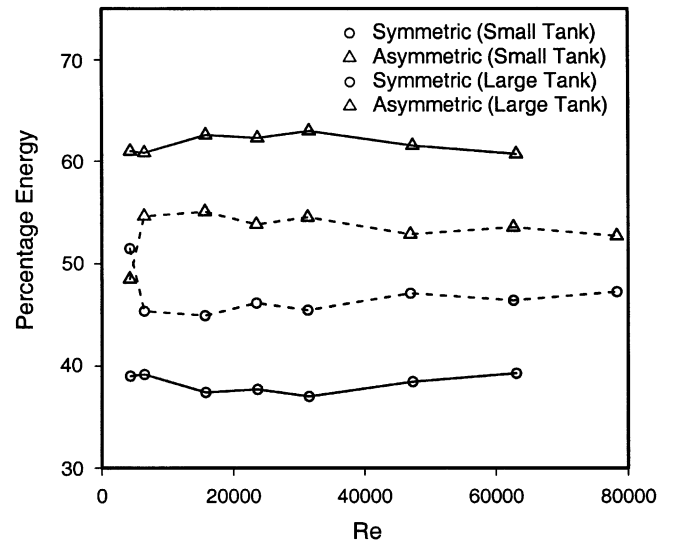


Fig. 16. Reynolds number dependence of the total energy content (shown as % energy) in the symmetric and the asymmetric modes for the small and large tank.

and normalized by the blade tip velocity, decreased with increasing Reynolds number and reached Reynolds number independence above $Re \approx 40,000$. The fluctuation of the out-of-plane velocity is significantly larger than that of either in-plane components. This suggests that the radial jet is the component most subject to unsteadiness.

A theoretical description of the jet flow based on thin shear layer approximation along with a simple model of the jet flow oscillation was considered. Estimates of rms and skewness of velocity seen by a fixed point in a frame rotating with the blade were obtained from the above simple model. In the region away from the influence of tip vortices, the actual rms and skewness of velocity obtained from the PIV measurements were qualitatively consistent with the model prediction. Thus, part of the measured velocity fluctuation can perhaps be attributed to the time-dependent oscillation of coherent impeller-induced flow components.

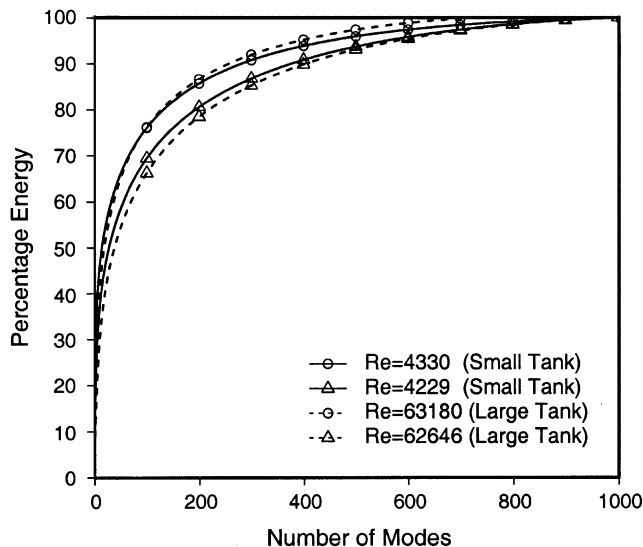


Fig. 17. Cumulative percentile energy in the dominant n modes for the small and the large tank for comparable Reynolds number.

The ensembles of fluctuation velocity fields were used to obtain the velocity eigenmodes using the method of snapshots. The spatial structure of the dominant eigenmode was observed to be similar in both the small and large tanks over the entire range of Reynolds number considered. The dominant mode (its out-of-plane velocity component) is asymmetric about the midplane of the tank and its energy content slowly decreases with increasing Re . The structure of the dominant symmetric mode also remains qualitatively similar for both the tanks over the range of Re considered. The total energy content of the symmetric and asymmetric modes is observed to be Reynolds number independent.

It is clear that the impeller-induced flow cannot be characterized by the mean component alone. The structure of instantaneous fluctuations is best characterized by the POD modes and the eigenvalues represent the strength of these fluctuations. For future reference, the POD modes and eigenvalue spectrum have been tabulated and made available for download at lcf.tam.uiuc.edu/~renchi/mixer/pod. This URL also contains an expanded set of figures showing higher order modes and a discussion of the data set to guide users.

Acknowledgements

This work was supported by a grant from National Science Foundation (CTS-9910543) and a gift from the Dow Chemical Company.

References

Costes, J., Couderc, J.P., 1988. Study by laser Doppler anemometry of the turbulent flow induced by a Rushton turbine in a stirred tank:

- influence of the size of the units I: mean flow and turbulence. *Chemical Engineering Science* 43, 2765.
- Derksen, J.J., Doelmann, M.S., Van Den Akker, H.E.A., 1999. Three dimensional LDA measurements in the impeller region of a turbulent stirred tank. *Experiments in Fluids* 27, 522.
- Desouza, A., Pike, R.W., 1972. Fluid dynamics and flow patterns in stirred tanks with a turbine impeller. *Canadian Journal of Chemical Engineering* 50, 15.
- Dong, L., Johansen, S.T., Engh, T.A., 1994. Flow induced by an impeller in an unbaffled tank—I. Experimental. *Chemical Engineering Science* 49, 549.
- Ducoste, J.J., Clark, M.M., Weetman, R.J., 1997. Turbulence in flocculators: effect of tank size and impeller type. *A.I.Ch.E. Journal* 43, 328.
- Escudie, R., Line, A., 2003. Experimental analysis of hydrodynamics in a radially agitated tank. *A.I.Ch.E. Journal* 49, 585.
- Escudie, R., Bouyer, D., Line, A., 2004. Characterization of trailing vortices generated by a Rushton turbine. *A.I.Ch.E. Journal* 50, 75.
- Holmes, P., Lumley, J.L., Berkooz, G., 1996. *Turbulence, Coherent Structures, Symmetry and Dynamical Systems*. Cambridge University Press, Cambridge.
- Kemoun, A., Lusseyran, F., Mallet, J., Mahouat, M., 1998. Experimental scanning for simplifying the model of a stirred-tank flow. *Experimental Fluids* 25, 23.
- Kim, K.C., 2004. Personal communication.
- Kolar, V., Filip, P., Curev, A.G., 1984. Hydrodynamics of a radially discharging impeller stream in agitated vessels. *Chemical Engineering Communications* 27, 313.
- Lamberto, D.J., Alvarez, M.M., Muzzio, F.J., 1999. Experimental and computational investigation of the laminar flow structure in a stirred tank. *Chemical Engineering Science* 54, 919.
- Mahouat, M., Cognet, G., David, R., 1989. Two component LDV measurements in a stirred tank. *A.I.Ch.E. Journal* 35, 1770.
- Mikhlin, S.G., 1957. *Integral Equations*. Pergamon Press, New York.
- Montante, G., Lee, K.C., Brucato, A., Yianneskis, M., 1999. An experimental study of double-to-single-loop transition in stirred vessels. *Canadian Journal of Chemical Engineering* 77, 649.
- Schaffer, M., Hofken, M., Durst, F., 1997. Detailed LDV measurements for the visualization of the flow field within a stirred tank reactor equipped with a Rushton turbine. *Transactions of the Institution of Chemical Engineers* 75 (Part A), 729.
- Sirovich, L., 1987. Turbulence and the dynamics of coherent structures. 1. Coherent structures, 2. Symmetries and transformations. *Quarterly of Applied Mathematics* 45, 561–582.
- Stoos, C.M., Calabrese, R.V., 1995. Mean velocity field relative to a Rushton turbine blade. *A.I.Ch.E. Journal* 41, 1.
- Sturesson, C., Theliander, H., Rasmuson, A., 1995. An experimental (LDA) and numerical study of the turbulent flow behavior in the near wall and bottom regions in an axially stirred vessel. *A.I.Ch.E. Symposium Series* 91, 102.
- van der Molen, K., van Maanen, H.R.E., 1978. Laser-Doppler measurements of the turbulent flow in stirred vessels to establish scaling rules. *Chemical Engineering Science* 33, 1161.
- Van't Riet, K., Smith, J.M., 1975. The trailing vortex system produced by Rushton turbine agitators. *Chemical Engineering Science* 30, 1093.
- Yoon, H.S., Sharp, K.V., Hill, D.F., Adrian, R.J., Balachandar, S., Ha, M.Y., Kar, K., 2001. Integrated experimental and computational approach to simulation of flow in a stirred tank. *Chemical Engineering Science* 56, 6635.
- Yoon, H.S., Hill, D.F., Balachandar, S., Adrian, R.J., Ha, M.Y., 2005. Reynolds number scaling of flow in a Rushton turbine stirred tank. Part I—Mean flow, circular jet and tip vortex scaling. *Chemical Engineering Science*, submitted, [10.1016/j.ces.2004.12.039](https://doi.org/10.1016/j.ces.2004.12.039).
- Yoon, H.S., Balachandar, S., Ha, M.Y., Kar, K., 2003. Large eddy simulation of flow in a stirred tank. *Journal of Fluids Engineering* 125, 486.